Effects of Spatial Sensitivity on Mass Sensing with Bulk Acoustic Mode Resonators

Arthur T. Zielinski[a*], Abhinav Prasad[b], Ashwin A. Seshia[b], Markus Kalberer[a], Roderic L. Jones[a]

[a] *Centre for Atmospheric Science, Department of Chemistry, University of Cambridge, Lensfield Road, Cambridge, CB2 1EW, UK*

[b] *The Nanoscience Centre, Department of Engineering, University of Cambridge, 11 JJ Thomson Avenue, Cambridge, CB3 0FF, UK*

Abstract

The spatial sensitivity of bulk acoustic mode resonators can influence calibrations when they are implemented as accurate mass sensors of surface-bound particles. A new spatial sensitivity model based on images of the resonator surface is introduced from early principles. The adsorption of particles was studied empirically by repeatedly drying particle laden droplets on the surface of two 3.14 MHz bulk acoustic mode resonators. Theoretical and experimental results were compared to identify three scenarios over the course of consecutive droplet evaporation with varying spatial sensitivity influences. Examining different surface treatments for the resonators revealed the hydrophilic surface to have a higher rate of particle stacking and conglomeration.

Keywords: Spatial Sensitivity; Bulk Acoustic Wave (BAW); Bulk Acoustic Mode Resonator; Particulate Mass Sensor; MEMS; Mathematical Modelling.

Highlights:

- Several spatial sensitivity models are introduced for particulate mass sensing.
- Comparison with experiments using evaporated particulate laden water droplets.
- Three sensitivity scenarios were identified for repeated mass addition.
- Hydrophilic surface shows propensity towards particle stacking and conglomeration.

1. Introduction

Micromechanical resonators have seen increased use in a range of inertial [1], temperature [2], and mass sensing [3] applications. Many mass sensing applications focus on uniform depositions [3,4], but a niche exists for dispersed aerosol particle sensing for environmental and health applications, with potentially non-uniform mass deposition. Atmospheric aerosols from anthropogenic or natural sources are key components of the climate system as they affect directly or via cloud processes the radiative budget of the atmosphere [5]. Negative health impacts of aerosol particles are well established based on correlations with particle mass and morbidity or mortality statistics [6].

Most current small-scale systems use optical methods [7] for detecting particles that cannot detect particles below 100 nm in diameter [8] (which may be responsible for most of the observed health effects [9,10]) and are typically expensive, complex, and can only estimate particle mass based on diameter. A desire for real time mass measurements led to the implementation of mechanical resonators as mass sensors. Early work by Chuan [11] replacing traditional impactor collection filters with a quartz crystal microbalance has since been extended to other micromechanical resonators. Black *et al.* [12] and Paprotny *et al.* [13] both used thin-film bulk acoustic resonators to measure particles collected via thermophoresis while Mehdizadeh *et al.* [14] employed thermally actuated resonators as part of a traditional impactor design. The above resonators have shown to offer highly sensitive detection of

[*] Corresponding author: Arthur T. Zielinski, arthur.zielinski@atm.ch.cam.ac.uk, Tel.: +44 1223 336345

particulate mass, but certain resonator geometries are susceptible to spatial variations in sensitivity [15,16] that must be accounted for when interpreting the resonator output.

A resonator can be modelled as a one-dimension mass-spring-damper system where the resonant frequency (f_0) is related to the effective mass (M_{eff}) and stiffness (K_{eff}) by:

$$f_0 = \frac{1}{2\pi}\sqrt{K_{\text{eff}} \big/ M_{\text{eff}}} \qquad \text{Eq. 1}$$

Mass addition to the device (effectively an increase in M_{eff}) results in a detectable frequency shift providing a means of mass sensing. Two of the most common resonator topologies are the flexural and bulk acoustic mode resonators [17]. This study focuses on bulk acoustic mode resonators due to their higher quality factors [18] as particle adsorption may degrade signal quality.

Uniform mass addition has previously been shown [19] to follow a general sensitivity model based on Sauerbrey's principle for a frequency shift Δf and mass addition Δm (assuming no change in stiffness):

$$\Delta f = -\frac{f_0}{2M_{\text{eff}}}\Delta m \qquad \text{Eq. 2}$$

The simple model, however, fails to account for the spatial sensitivity of the resonator. Previous studies by Campanella *et al.* [20] have modelled spatial dependencies in thin-film bulk acoustic-wave resonators (FBARs). Their results highlight the importance of spatial sensitivity in microresonators while also discussing the influence of deposition area. The following study develops a spatial sensitivity model in the context of particulate adsorption from a liquid medium for the purpose of mass sensing using bulk acoustic mode resonators. The model can be used to study the mass of particles in liquid biological samples or to study the deposition of particles from a gaseous medium (by removing the influence of the liquid) for more relevant atmospheric measurement studies. The theoretical model was compared with experimental results using square bulk acoustic mode single-crystal silicon microelectromechanical systems (MEMS) resonators to show three different stages of particle adsorption based on residue formation after evaporation. Work focused on the symmetric square-extensional mode but the method can be expanded to different geometries and modes.

2. Description of resonators

Bulk mode resonators are defined to have full body contraction and extension. For a square, corner-anchored resonator the two commonly excited in-plane vibration modes are the square-extensional (SE) and wine glass (WG) – or Lamé – modes. The SE mode is characterised by symmetric extension/contraction along orthogonal axes producing a node at the resonator centre and antinodes at the corners. The WG mode is characterised by asymmetric extension/contraction along orthogonal axes producing nodes at the centre and corners of the resonator and antinodes at the edge midpoints. Contour plots of displacement for these modes are shown in Fig. 1. The SE mode was the focus of this study as it is simpler to model and can be implemented with piezoresistive sensing to increase the motional signal [21]. The theoretical resonant frequencies for the experimental resonator size (1400 μm side length) are 3.140 MHz and 2.949 MHz for SE and WG modes, respectively. The experimental resonators were silicon-on-insulator (SOI) devices fabricated using Multi-User MEMS Processes (MUMPs) produced by MEMSCAP [22]. Dimensions and properties of the resonators for the SE mode are shown in Table 1.

The symmetric in-plane displacements for SE mode can be described as follows [16] for $x \in [-L/2, L/2]$ and $y \in [-L/2, L/2]$:

$$u_x(x,t) = U_0 \sin\left(\frac{\pi x}{L}\right)\sin(\omega t) \quad \text{Eq. 3a}$$

$$u_y(y,t) = U_0 \sin\left(\frac{\pi y}{L}\right)\sin(\omega t) \quad \text{Eq. 3b}$$

where U_0, L, and ω are the maximum displacement, resonator side length, and modal frequency of the resonator in the x and y directions at time t. Note that the maximum displacement, U_0, has no effect on the sensitivity of the device. The above equations provide the basis of the spatial sensitivity model.

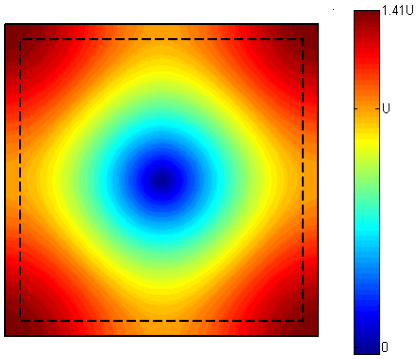

(a)

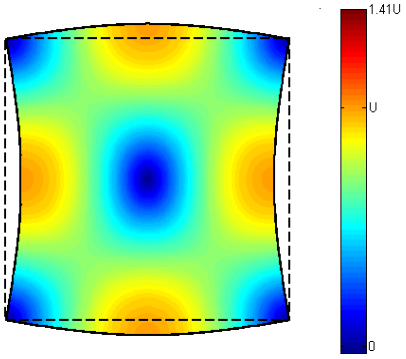

(b)

Fig. 1. Contour plots of total displacement (as a fraction of maximum unidirectional displacement, *U*) with deformed (solid line) and undeformed (dashed line) mode shapes for the (a) square extensional mode and (b) wine glass mode.

Table 1 Nominal dimensions and characteristics for the SE mode. Resonators were electrostatically forced and piezoresistively sensed.

Parameter	Unit	Value
Resonator thickness	μm	25
Resonator side length	μm	1400
Capacitance gap	μm	2
Effective mass	μg	114
Effective spring constant	N μm^{-1}	44.4
Natural frequency	MHz	3.140
DC bias	VDC	60
AC power	dBm	0

3. Theoretical sensitivity models

The spatial sensitivity of a bulk mode resonator is caused by the non-uniform displacement across the resonator body as highlighted by Fig. 1a. For the SE mode, a point mass placed at a corner – an antinode – would experience larger displacements and velocities than an identical point mass placed near the node at the centre of the resonator. Higher velocities result in a larger kinetic energy contribution to the system leading to larger frequency shifts.

The Rayleigh-Ritz method can be used, assuming negligible damping, to estimate the resonant frequency of a resonator. The approach assumes the summation of kinetic and potential energies of the system remains constant. The maximum potential and kinetic energies would then be equal and occur when the other is zero. It is possible to extend this result for the inclusion of a new mass to the resonator via an additional kinetic energy term assuming negligible stiffness change (*i.e.* the local resonator mass increases without modifying the elastic behaviour).

Three mass addition scenarios were considered in increasing levels of complexity: point mass addition, circular/annular mass addition, and squircular mass addition. The point mass scenario assumes the mass is confined to an infinitesimally small area on the resonator and serves as a proof-of-concept calculation. The circular/annular scenario assumes the mass is spread over a circular (or annular) area with known outer and inner radii. This scenario serves to mimic the "coffee-ring" effect which involves higher concentrations of particle collection along the outer edges of residue [23]. The squircular (a combination of a square and a circle) scenario is meant to account for droplets large enough to interact with the resonator edges. Both the circular/annular and squircular models assumed centred residues but can be modified to account for positional offsets as shown below with a modular squircular approach.

The following derivations are for the SE mode only.

3.1 No mass addition

The no mass addition scenario serves to calculate the initial resonant frequency of a resonator. Treating the resonator as a simple mass spring system, the kinetic and potential energies are:

$$KE = \tfrac{1}{2} M_{\text{eff}} \dot{u}^2 \qquad \text{Eq. 4a}$$

$$PE = \tfrac{1}{2} K_{\text{eff}} u^2 \qquad \text{Eq. 4b}$$

where KE and PE are the kinetic and potential energies for a resonator with effective mass M_{eff}, effective stiffness K_{eff}, local displacement u, and local velocity $\dot{u}$.

For a resonator vibrating at the SE mode, the effective mass and stiffness are given by [16]:

$$M_{\text{eff}} = \rho_{\text{Si}} h L^2 \qquad \text{Eq. 5a}$$

$$K_{\text{eff}} = \pi^2 E_{\text{Si}} h \qquad \text{Eq. 5b}$$

where ρ_{Si}, h, L, and E_{Si} are the density, thickness, side length, and Young's modulus of the resonator, respectively.

The maximum kinetic and potential energies can be solved using Eq. 3 and Eq. 4 to yield:

$$KE_{\max} = \tfrac{1}{2} M_{\text{eff}} \left(U_0 \omega_0\right)^2 \qquad \text{Eq. 6a}$$

$$PE_{\max} = \tfrac{1}{2} K_{\text{eff}} U_0^2 \qquad \text{Eq. 6b}$$

Equating the above equations, as per the Rayleigh Ritz method, yields the well-known result:

$$\omega_0 = \sqrt{\frac{K_{\text{eff}}}{M_{\text{eff}}}} \qquad \text{Eq. 7}$$

3.2 Point mass addition

An additional mass, *m*, can be added to the system through a kinetic energy term. If the mass is placed at a location (*x*, *y*) then the maximum energy equality becomes the following (using Eq. 3 and Eq. 4 as before):

$$\left(U_0\omega_0\right)^2\left[M_{\text{eff}} + m\left(\sin^2\left(\frac{\pi x}{L}\right)+\sin^2\left(\frac{\pi y}{L}\right)\right)\right] = K_{\text{eff}}U_0^2 \qquad \text{Eq. 8}$$

The new resonant frequency, $\omega_{0,\text{pm}}$, is:

$$\omega_{0,\text{pm}} = \sqrt{\frac{K_{\text{eff}}}{M_{\text{eff}} + m\left(\sin^2\left(\frac{\pi x}{L}\right)+\sin^2\left(\frac{\pi y}{L}\right)\right)}} \qquad \text{Eq. 9}$$

Sauerbrey's equation, Eq. 10, estimates the frequency shift for mass and stiffness addition.

$$\Delta f = \frac{1}{2}\left(\frac{\Delta k}{K_{\text{eff}}} - \frac{\Delta m}{M_{\text{eff}}}\right) f_0 \qquad \text{Eq. 10}$$

If the stiffness change is negligible (*i.e.* $\Delta k \approx 0$), the sensitivity factor, *S*, can be solved to satisfy $\Delta f = S f_0$ for an added mass $\Delta m = m\,[\sin^2(\pi x/L) + \sin^2(\pi y/L)]$ located at a given (*x*, *y*) position:

$$S_{\text{pm}} = -\frac{m\left(\sin\left(\frac{\pi x}{L}\right)^2+\sin\left(\frac{\pi y}{L}\right)^2\right)}{2\rho_{\text{Si}}hL^2} \qquad \text{Eq. 11}$$

Eq. 11 is valid for small mass additions and positions within $x \in [-L/2, L/2]$ and $y \in [-L/2, L/2]$. Note that sensitivity is typically an intensive property for a given mode shape whereas the above defined sensitivity factor is an extensive property.

3.3 Circular/annular mass addition

For a mass spread over a significant area, the additional kinetic energy term must be integrated across its entire volume. For an infinitesimally small slice of a quarter circle with mass *dm*, the kinetic energy *dKE* is:

$$dKE = \tfrac{1}{2}\dot{u}^2\,dm \qquad \text{Eq. 12a}$$

$$dKE = \tfrac{1}{2}\rho_{\text{add}}\delta\dot{u}^2\,dA \qquad \text{Eq. 12b}$$

where ρ_{add}, δ, and *dA* are the density, thickness, and area of the slice. Note that this assumes uniform thickness and mass distribution across the area. Due to the linearity of integrals, an annular mass can be solved by simple subtraction following the identity:

$$\int_{r_\text{i}}^{r_\text{o}} f(x)dx = \int_0^{r_\text{o}} f(x)dx - \int_0^{r_\text{i}} f(x)dx \qquad \text{Eq. 13}$$

Fig. 2 shows the quarter circle of radius *r* to be integrated in order to solve Eq. 12.

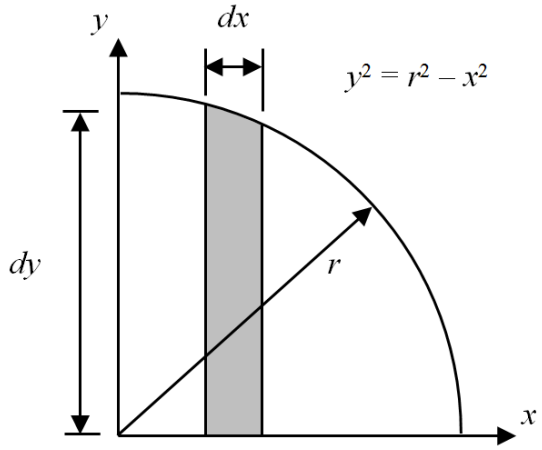

Fig. 2. Quarter circle of radius r with integration slice of area dA shaded.

Based on the figure the area dA is:

$$dA = \sqrt{r^2 - x^2}\,dx \qquad \text{Eq. 14}$$

Integrating the quarter circle in the x-direction from $x = 0 \rightarrow r$ gives the following (assuming $r \leq L/2$):

$$KE = \frac{1}{2}\rho_{\text{add}}\delta U_0^2 \cos^2(\omega t) I(r) \qquad \text{Eq. 15}$$

where

$$I(r) \equiv \int_{x=0}^{r} \sin^2\left(\frac{\pi x}{L}\right)\sqrt{r^2 - x^2}\,dx \qquad \text{Eq. 16a}$$

$$I(r) = \ldots = \frac{r}{8}\left(\pi r - L J_1\left(\frac{2\pi r}{L}\right)\right) \qquad \text{Eq. 16b}$$

and $J_1(x)$ is the Bessel function of the first kind.

Based on the symmetry of the SE mode, the total kinetic energy for a full annulus (of inner and outer radii r_i and r_o, respectively) in both directions is given by the following. Note that setting $r_i = 0$ yields the result for a circle.

$$KE = 4\rho_{\text{add}}\delta U_0^2 \omega^2 \cos^2(\omega t)\left[I(r_o) - I(r_i)\right] \qquad \text{Eq. 17}$$

The maximum energy equality is then:

$$(U_0\omega_0)^2\left[M_{\text{eff}} + 4\rho_{\text{add}}\delta U_0^2\omega_0^2\left[I(r_o) - I(r_i)\right]\right] = K_{\text{eff}}U_0^2 \qquad \text{Eq. 18}$$

and the resonant frequency and sensitivity factor are:

$$\omega_{0,\text{an}} = \sqrt{\frac{K_{\text{eff}}}{M_{\text{eff}} + 4\rho_{\text{add}}\delta\left[I(r_o) - I(r_i)\right]}} \qquad \text{Eq. 19}$$

$$S_{\text{an}} = -\frac{2\rho_{\text{add}}\delta\left[I(r_o) - I(r_i)\right]}{\rho_{\text{Si}}hL^2} \qquad \text{Eq. 20}$$

Eq. 20 is valid for small mass additions and residue outer radii $r_o \leq L/2$.

3.4 Squircular mass addition

A squircle is a geometric shape that shares properties between a square and a circle and it is a special case of the Lamé curve or superellipse. One possible definition [24] of the squircle in the *x*-*y* plane utilises a squareness factor, *s*, that ranges from 0 (circle) to 1 (square). A circle, therefore, is a subset of the general squircle shape. The definition, when centred at the origin, is given below and plotted in Fig. 3 for varying values of *s* and a constant *k*.

$$s^2 \frac{x^2}{k^2}\frac{y^2}{k^2} - \left(\frac{x^2}{k^2} + \frac{y^2}{k^2}\right) + 1 = 0 \qquad \text{Eq. 21}$$

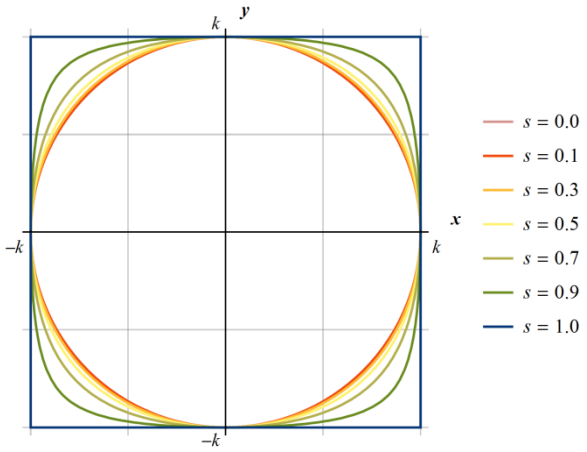

Fig. 3. Centred squircle geometry for varying squareness parameter values (*s*) with constant *k* based on the definition by Guasti [24]. Note that the *s* = 0.0 and *s* = 0.1 cases nearly completely overlap.

Following the same procedure for the circle in Section 3.3, the sensitivity factor can be shown to be:

$$S_{sq} = -\frac{2\rho_{add}\delta P(k)}{\rho_{Si} h L^2} \qquad \text{Eq. 22}$$

where

$$P(k) \equiv k \int_{x=0}^{k} \sin^2\left(\frac{\pi x}{L}\right) \sqrt{\frac{\left(x^2/k^2\right)-1}{s^2\left(x^2/k^2\right)-1}}\, dx \qquad \text{Eq. 23}$$

The function $P(k)$ does not have an analytical solution, unlike $I(r)$, and requires numerical methods to be solved. Eq. 22 is valid for small mass additions and residue sizes $k \leq L/2$ and squareness parameters ranging from $0 \leq s < 1$.

A summary of the derived theoretical model results is given in Table 2.

Table 2 Summary of theoretical sensitivity models for a point mass at location (x, y), centred circular/annular mass, and centred squircular mass.

Residue Shape	Sensitivity Factor, S
Point mass	$-\dfrac{m\left(\sin\left(\dfrac{\pi x}{L}\right)^2+\sin\left(\dfrac{\pi y}{L}\right)^2\right)}{2\rho_{\mathrm{Si}}hL^2}$
Centred circle/annulus	$-\dfrac{2\rho_{\mathrm{add}}\delta\left[I(r_{\mathrm{o}})-I(r_{\mathrm{i}})\right]}{\rho_{\mathrm{Si}}hL^2}$
Centred squircle	$-\dfrac{2\rho_{\mathrm{add}}\delta P(k)}{\rho_{\mathrm{Si}}hL^2}$

3.5 Modular approach

While the above squircle definition is a close approximation to the shape remaining after the evaporation of droplets in contact with the resonator edges (Fig. 4a), a combination of a square and a circle provides a more accurate fit as it accounts for the longer and non-uniform linear portions along the resonator edges caused by surface tension. This procedure is also simpler for image processing and effectively allows for individual squareness parameters at each corner due to any off-centre alignment.

The modular approach involves fitting a square to the resonator and a circle to the residue, as seen in Fig. 4b, with the origin placed at the centre of the resonator. The circle may extend past the resonator, be off centre, and allows up to eight intersection points to exist scenario (*i.e.* the four rounded corners of the squircle shape must exist). A narrowed contour, governed by a uniform offset from the outer shape, then splits the residue into inner and outer regions (Fig. 4c). Splitting the residue allows the model to account for the "coffee-ring" effect by distributing different masses in each region while still assuming homogenous density within both.

Once the residue is split, the intersection points are calculated and the integration regions (up to twenty in each direction) are defined for both the x- (Fig. 4d) and y-directions. The integration regions are bounded by the exterior curve (either an arc or a line), the interior curve (either an arc or a line), or the x- or y-axis between the intersection points. Eq. 12b is then integrated over these regions and used to solve for the sensitivity factor.

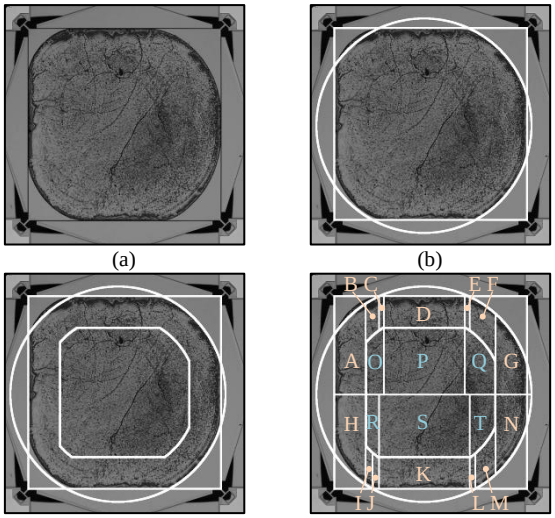

Fig. 4. Processing steps for modular approach showing (a) the original, aligned image, (b) the fitted square (resonator) and circle (residue), (c) the contour that splits the residue, (d) the integration regions for the *x*-direction in the outer (labelled A through N) and inner (labelled O through T) regions. The interior contour and all integration regions are for illustrative purposes only (with outer regions exaggerated for clarity) to describe the method. Similar regions are used for *y*-direction.

4. Model intercomparison discussion

The point mass model provides a means to examine the relative effect of mass placement but does not accurately represent the effect of droplet evaporation which consists of a dispersion of particles. Note that the maximum sensitivity, located at the corner antinodes, of the point mass model is twice that of the theoretical maximum given by Eq. 2.

A comparison of annular ring thicknesses yields the implications of the "coffee-ring" effect. As the thickness of the ring decreases the mass distribution becomes more concentrated towards the outer radius of the residue, r_o. Referring to Fig. 1a, this results in more mass located at areas of high velocity thus increasing the mass loading. The results of running the circular/annular model at various thicknesses, t, for a constant mass is summarised in Fig. 5. When $r_o = L/2$ the resonator is more sensitive for small thicknesses ($t < 0.5r_o$) than the uniform distribution case due to the concentrated placement of the mass as seen previously with the point mass model. The WG mode shape (Fig. 1b) would result in more pronounced sensitivity inflation since the antinodes would be better aligned with the ring.

Adjusting the squareness factor can simulate the sensitivity effects of placing a large droplet (or a series of droplets) as discussed above. Fig. 6 shows the sensitivity factors relative to the uniform thin film deposition case for different sizes (k) and squareness parameter values (s). The most representative comparison occurs when $k = L/2$ since before the residue touches the resonator edge the residue would remain circular. Note that as k approaches the size of the resonator, $L/2$, the $s = 0.0$ cases matches the full circle case ($t = 1.0r_o$) in Fig. 5 and the $s = 1.0$ case matches the uniform thin film case as expected. Based on the experimental studies discussed below, the average squareness parameter for the hydrophilic resonator was estimated to be $s = 0.74 \pm 0.02$ based on 16 processed images with visible residue contact along the resonator perimeter. This value implies modelling the experimental results as squircles is significant.

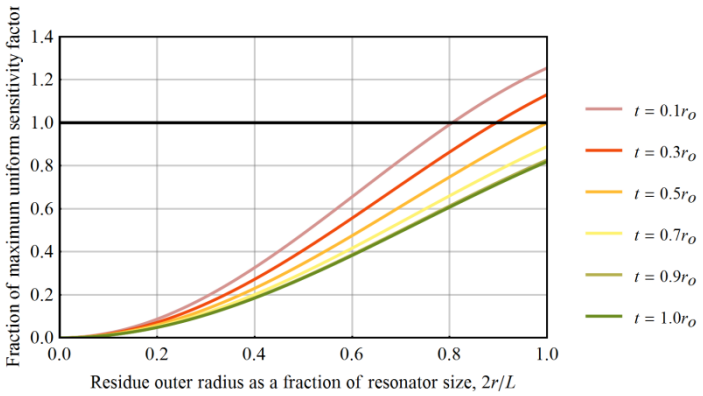

Fig. 5. Sensitivity factors relative to a uniform thin film deposition for different annulus thicknesses, t, as fractions of the outer radius ranging from $t = 0.1r_o$ (thin ring) to $t = 1.0r_o$ (full disc). Mass kept constant for all sizes (*i.e.* homogenous density varied with changing r_o and t). For small thicknesses ($t < 0.5r_o$) the sensitivity is higher than theoretical maximum as the mass approaches the antinodes only.

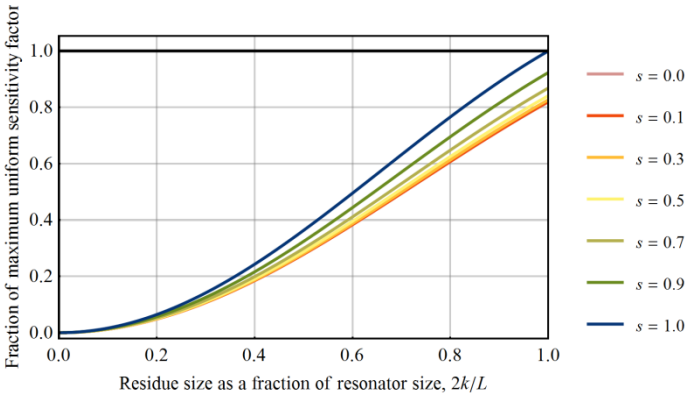

Fig. 6. Sensitivity factors relative to a uniform thin film deposition for different squareness parameter values ranging from $s = 0.0$ (a circle) to $s = 1.0$ (a square). Mass kept constant for all sizes (*i.e.* homogenous density varied with changing k).

5. Experimental studies

A set of experiments were conducted to evaluate the accuracy of the modular approach for calculating sensitivity factors.

5.1 Experimental procedure

0.5 µL droplets containing a 2.2 ± 0.1 ng µL^{-1} suspension of 296 ± 6 nm polystyrene latex (PSL) particles (Nanosphere Size Standards, Thermo Fisher Scientific) in High Performance Liquid Chromatography (HPLC) grade water were manually deposited onto 1400 µm square resonators and evaporated in a vacuum chamber. Two suspended resonators, of identical design, were treated to become either hydrophilic or hydrophobic. The hydrophilic surface was produced with low-power O_2 RF plasma (to remove any hydrophobic coatings) while the hydrophobic surface was created using a perfluorodecyltrichlorosilane (FDTS) self-assembled monolayer which has previously been implemented with MEMS surfaces [25].

Droplets were placed sequentially on each resonator and evaporated in a vacuum chamber before measuring the resonant frequency while still under vacuum. The resonator surfaces were optically imaged after each measurement. Twenty and ten drops were placed on the hydrophilic and hydrophobic resonators, respectively. The frequency output from the resonator was measured using a network analyser (Agilent 4396B Network/Spectrum/Impedence Analyzer) via piezoresistive sensing of a one-port capacitive

forcing arrangement (Fig. 7). Frequency measurements, taken over a span of 1 kHz centred at the peak, were recorded after a set time to minimise temperature drift induced by piezoresistive sensing and allow for pressure stabilisation within the chamber. The experimental sensitivity factor, S_i, discussed in subsequent sections was calculated for each droplet i based on a measured frequency, f_i, following the definition $S_i = (f_i - f_0)/f_0$.

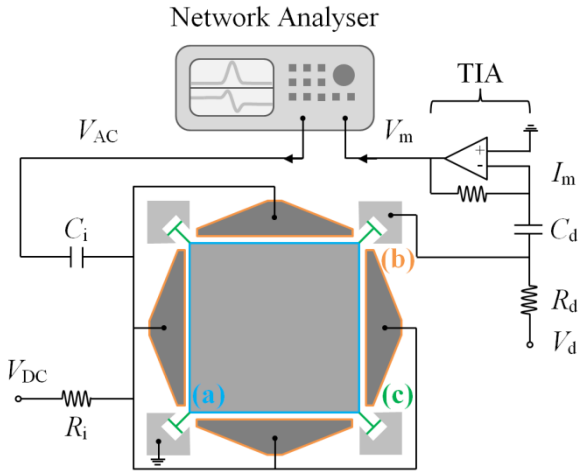

Fig. 7. Circuit schematic for one-port capacitive forcing with piezoresistive sensing highlighting the (a) resonator, (b) electrodes, and (c) anchors (adapted from [26]). An input voltage consisting of AC (V_{AC}) and DC (V_{DC}) components is sent to actuate all four electrodes. The output motional current (I_m) is then sensed through one of the anchors with the diagonally opposite anchor being grounded. The motional current is then passed to the network analyser via a transimpedence amp (TIA) to measure the S_{21} parameter.

The above method was previously shown [15] to provide consistent (yet elevated) mass addition due to the presence of contaminant particles which was accounted for based on larger scale mass experiments as discussed in Section 5.3.

5.2 Model comparisons

Each image was analysed using the modular approach described in Section 3.5 to estimate the relative frequency shift induced by each droplet. Image processing was performed using simple geometric relations and the GNU Image Manipulation Program (GIMP) [27]. The "coffee-ring" thicknesses were 0.024 and 0.040 of the effective residue radius for hydrophilic and hydrophobic surfaces, respectively, based on average values for each set of images as analysed through GIMP. Following studies by Yunker *et al.* [23], which corroborate the "coffee-ring" thicknesses above, 98.5% of the total mass was distributed in the "coffee-ring" for each model run. The total mass per droplet used in the model (approximately 5.2 ng) included factors accounting for contaminants (further explained in Section 5.3) in the solution and potentially trapped water between closely packed particles. The model assumes the total added mass is redistributed after each droplet following the "coffee-ring" distribution.

Recalling that the theoretical model assumes homogenous distributions, it should be recognised that the any heterogeneity of the mass distribution could influence the following comparisons. Modelling this heterogeneity is quite difficult, and the true response depends on the mass location relative to the mode shape in a similar fashion to Fig. 5 and Fig. 6.

The comparison between measured (with capacitive feedthrough removed following Lee *et al.* [17]) and modelled results on a per droplet basis are shown in Fig. 8 while a direct comparison via correlation plots is shown in Fig. 9. Both correlation plots show strong correlation with r^2 values above 98% and slopes implying gain errors on the order of 1.5. Slopes greater than 1 suggest the existence of additional unexpected mass, on the order of 2 to 3 ng, that may be due in part to discrepancies in solution preparation procedures between resonator testing and the larger scale microbalance studies (Section 5.3).

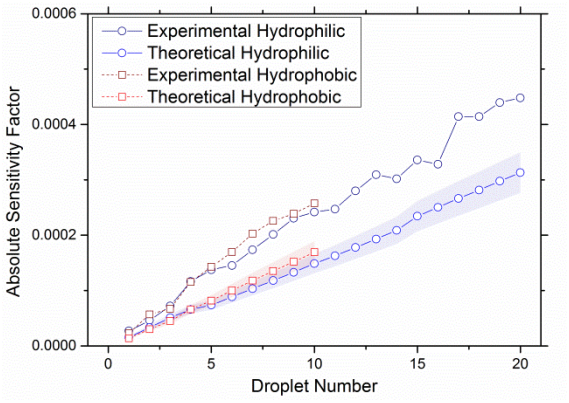

Fig. 8. Absolute experimental and theoretical sensitivity factors for both resonator surface treatments on a per droplet basis. Experimental results show a distinctly increased slope implying more mass was added than expected. The theoretical model assumes a mass addition of 5.2 ng per droplet (including contaminants). Filled areas represent 95% confidence interval of fit.

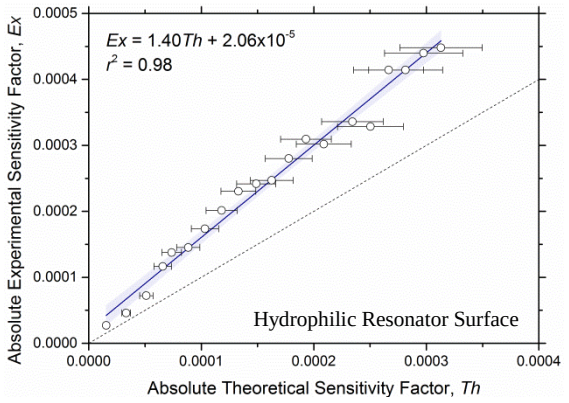

(a)

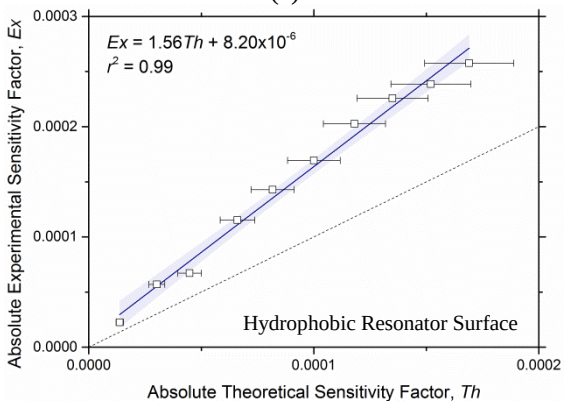

(b)

Fig. 9. Correlation plots for (a) hydrophilic and (b) hydrophobic resonators between experimental and theoretical sensitivity factors showing a strong linear relationship with a small slope and a factor of approximately 1.5 difference between the model and experimental results. Experimental results have capacitive feedthrough analytically removed. The theoretical model assumes a mass addition of 5.2 ng per droplet (including contaminants). Filled areas represent 95% confidence interval of fit.

Inconsistent slopes between the resonators could imply differences in mass distribution, residue thickness, or particle stacking (as discussed in Section 5.4). Manufacturing discrepancies from nominal resonator dimensions may also have a minor influence on the slopes. The non-zero *y*-intercepts in the correlations highlight the uncertainty in the slopes as they should ideally be zero. Note that the *y*-intercept for the hydrophobic resonator is within zero when considering the 95% confidence interval.

Using the slopes from each correlation to orientate data on the same scale, the experimental and theoretical relative frequency shifts (*i.e.* sensitivity factors) were plotted to show the drop-by-drop trends in Fig. 10. There are three general scenarios seen during the deposition of particles: residue growth, uniform mass addition, and particle stacking.

The residue growth scenario is described by an increasing residue radius over sequential drops. This scenario experiences the largest spatial sensitivity as the droplet is both expanding and adjusting its location as particles are rearranged. Fig. 11 shows the residue growth and highlights a transition after the fifth droplet for both resonators after which the radius remains stable. Fig. 12 shows a selection of images of the resonator surface corresponding to the initial droplet (Drop 1), the transition (Drop 5), and the final residue (Drop 20, 10) for both resonators. Note that the general residue shape does not change between the transition and final images but there is a distinct increase in particle concentration. The concept of spatial sensitivity dictates that the slope magnitude should reduce after the transition (*i.e.* the fifth droplet) as the frequency shift will solely be mass based. Experimental results corroborate this expectation as the slope magnitudes reduced from $(2.9 \pm 0.6)\times10^{-5}$ droplet^{-1} to $(2.1 \pm 0.2)\times10^{-5}$ droplet^{-1} and from $(3.0 \pm 0.5)\times10^{-5}$ droplet^{-1} to $(2.1 \pm 0.4)\times10^{-5}$ droplet^{-1} for the hydrophilic and hydrophobic resonators at confidence levels of 90% and 80%, respectively.

After the transition, there is a scenario of uniform mass addition which the model expects to be relatively constant. This holds true for the experimental hydrophobic data, but the hydrophilic data shows significant fluctuations past the tenth droplet. The expected cause of these fluctuations is the vertical stacking of particles after each droplet is evaporated as the higher stacked particles will have diminished energy influences based on their attachment stiffness. Particle stacking was previously shown [15] to take place during droplet deposition. Since the theoretical model assumes a constant energy contribution per mass added it does not account for these fluctuations.

The spatial sensitivity model provides the most information prior to the residue stabilising in shape and accounts for some of the experimental fluctuations seen during this region. For example, the shift between the third and fourth drop on the hydrophobic resonator is well captured by the model. The fourth hydrophobic droplet saw a sudden residue expansion, captured in the residue sizes from Fig. 11, resulting in the substantial frequency shift. In general, the sensitivity model appears to be applicable regardless of surface treatment as overall trends were consistent and local trends within the residue growth region followed the experimental results well.

An additional detail presented by Fig. 10 is that once the gain error is accounted for the experimental results and theoretical results follow quite well (and generally within uncertainty) implying that the main discrepancy is likely due to a consistent unaccounted mass in each droplet.

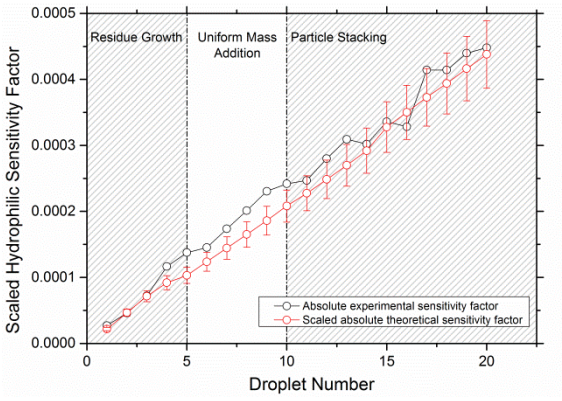

(a)

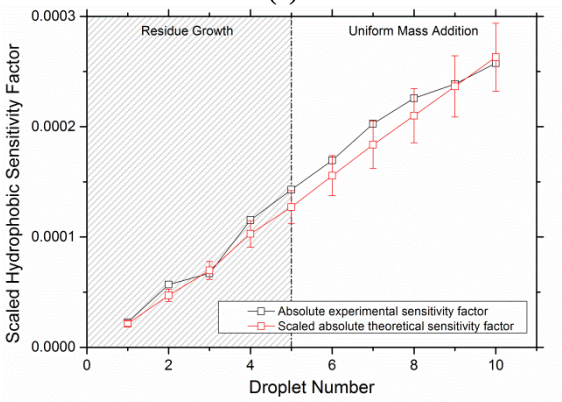

(b)

Fig. 10. Sensitivity factors on a per droplet basis relative to original, unloaded resonant frequency using experimental and theoretical results for the (a) hydrophilic and (b) hydrophobic resonators. Theoretical results adjusted to the experimental scale using correlation slopes as given in Fig. 9.

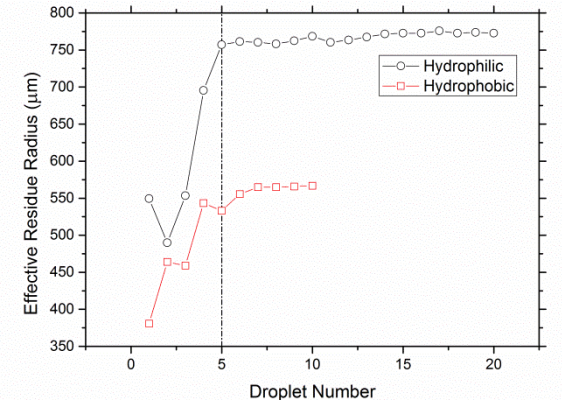

Fig. 11. Residue radius growth rate per droplet. Radius stabilises for both resonators (hydrophilic and hydrophobic) at approximately the fifth droplet. The hydrophilic radius is based on the modular approach and describes a squircle rather than a perfect circle.

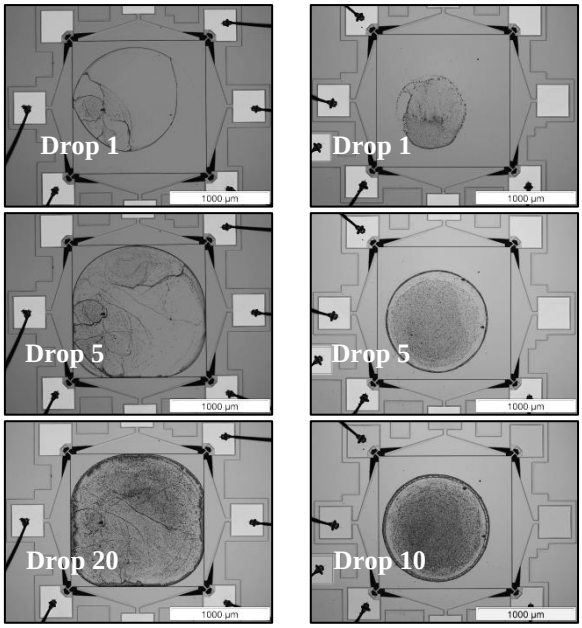

(a) (b)

Fig. 12. Selected images after measurement for (a) hydrophilic and (b) hydrophobic resonators. The first drop shows the start of the residue growth for both resonators. The fifth drop for both resonators is the point when the residue size stopped significantly growing as per Fig. 11. The twentieth and tenth drop for the hydrophilic and hydrophobic resonators, respectively, show the final resonator surfaces with a similar area to the fifth drop but noticeably larger concentrations of particles.

5.3 Examining contamination factor

Larger scale mass experiments were conducted, using a mechanical microbalance (M5, Mettler Inc.), to quantify the additional mass deposited when using a suspension of PSL particles and HPLC grade water. The procedure separated a set of twelve vials, previously cleaned via methanol sonication and baking, into three groups: six vials for a PSL particle and HPLC grade water solution, three vials for HPLC grade water only, and three vials left as a control (*i.e.* empty). Volumes of 5 mL were pipetted into each non-control vial and left to evaporate under a nitrogen air flow before measuring the mass change. Three different concentrations of PSL particles were used in two different sets of vials. In the first vial set, a concentration of 27 ± 1 µg mL^{-1} was used for a single measurement. In the second vial set, three measurements using a concentration of 54 ± 3 µg mL^{-1} were followed by two measurements using a concentration of 139 ± 7 µg mL^{-1}.

The results of these experiments showed a significant deviation from a 1:1 relationship between expected and actual PSL particle mass as shown in Fig. 13. Similarly, Fig. 14 shows significant contamination from the water. A deposited mass correction can be completed assuming a percentage contamination associated with PSL particle mass (slope from Fig. 13) and a volume based contamination for the HPLC grade water measurements (slope from Fig. 14). The correction equation based on these slopes is presented in Fig. 15 with the original data points included to show good agreement. Extending this relationship to the original 0.5 µL droplets containing 1.1 ng of PSL particles, the corrected mass is 4.0 ± 0.4 ng with approximately 2/3 of the mass coming from water contamination. SEM images, shown in Fig. 16, corroborate that both the stock PSL solution and HPLC grade water contain contaminants. Note that surfactants in the stock PSL particle solution were expected to only make up 0.142% of the total PSL particle-related mass.

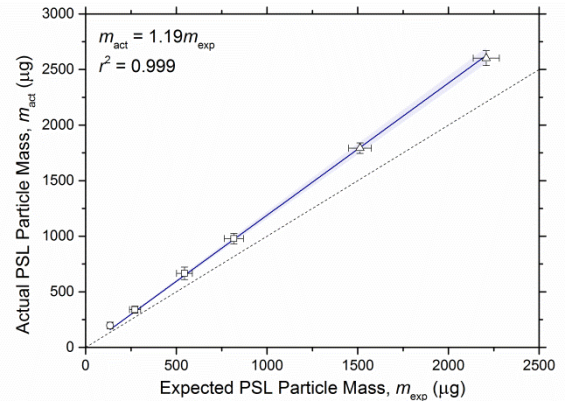

Fig. 13. Correlation plot between actual and expected PSL particle mass addition. Expected mass is based on solution concentrations; actual mass is the mass difference between PSL particle-containing and water only vials. A strong linear relationship implies 19% more mass was added than expected from the PSL solution alone (does not account for water contamination). Symbols correspond to PSL concentrations (○, □, and Δ describe 27 ± 1 µg mL^{-1}, 54 ± 3 µg mL^{-1}, and 139 ± 7 µg mL^{-1}, respectively). Filled area shows 95% confidence interval of fit. Dashed line represents 1:1 ratio.

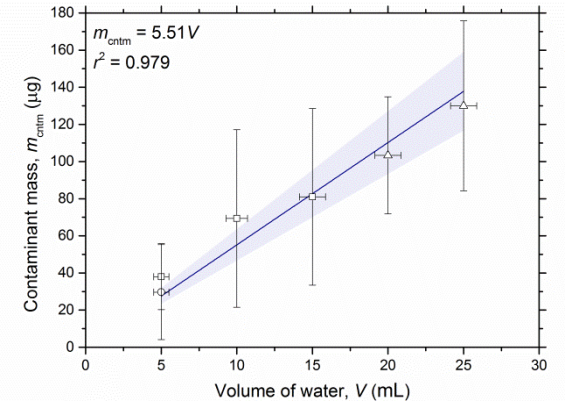

Fig. 14. Correlation plot between water contamination mass and deposited HPLC grade water. Contamination mass is based on the mass difference between water only vials and the control vials. A strong linear relationship implies 5.51 µg of contaminants in the water is added per mL. Symbols correspond to PSL concentrations (○, □, and Δ describe 27 ± 1 µg mL^{-1}, 54 ± 3 µg mL^{-1}, and 139 ± 7 µg mL^{-1}, respectively). Filled area shows 95% confidence interval of fit.

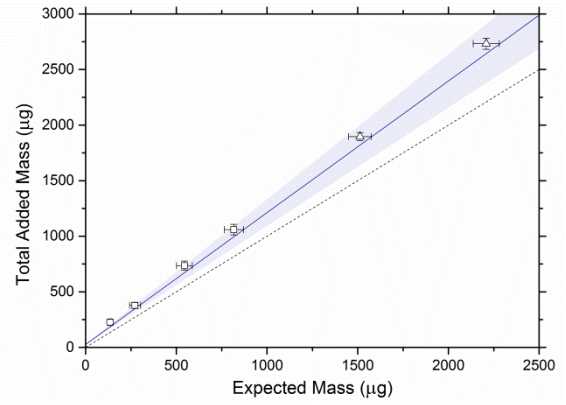

Fig. 15. Correlation plot between the total added mass and expected (*i.e.* PSL particle) mass. Fitted line describes predictive equation (with 95% confidence interval) based on slopes from Fig. 13 and Fig. 14. Symbols correspond to PSL concentrations (○, □, and Δ describe 27 ± 1 µg mL^{-1}, 54 ± 3 µg mL^{-1}, and 139 ± 7 µg mL^{-1}, respectively). Dashed line represents 1:1 ratio.

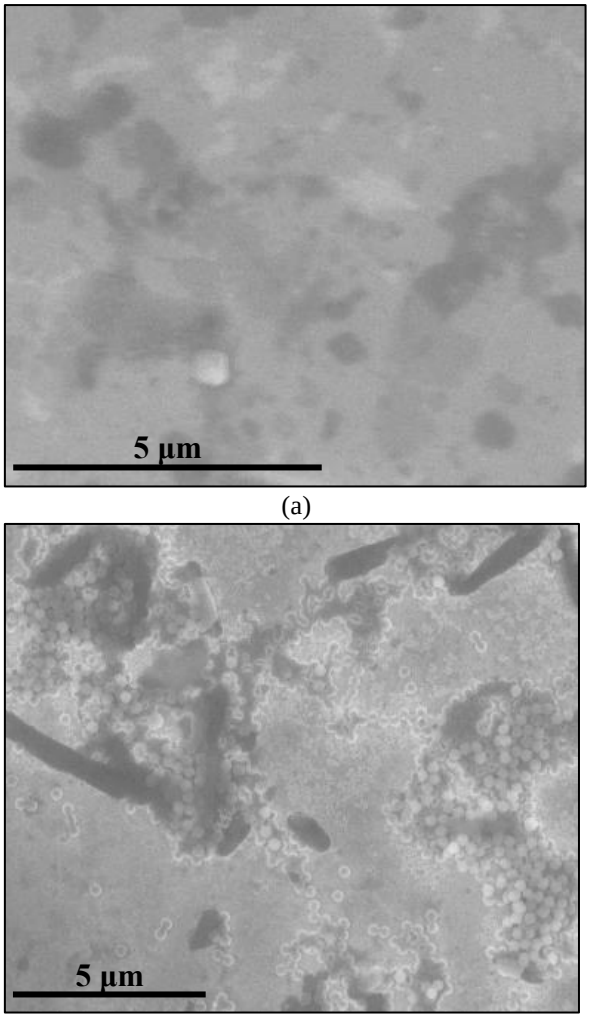

Fig. 16. SEM images of an untreated, hydrophilic silicon resonator surface with evaporated (a) HPLC grade water only and (b) PSL particles and HPLC grade water. The contamination seen in (a) also covers the surface of the resonator surface in (b). The dark, cylindrical particles in (b) are contaminants (PSL particles are white and spherical).

5.4 Comparing Hydrophilic and Hydrophobic Coatings

Based on the early model runs shown in Fig. 6 it would be expected that the hydrophilic sensitivity would be higher than the hydrophobic sensitivity since the residue has reached the more sensitive regions of the resonator. However, as shown in Fig. 17, both the experimental and theoretical results show disagreement with this expectation. Past the residue growth region, the hydrophilic sensitivity is approximately 90% of the hydrophobic sensitivity which is partially explained by the assumptions made for mass distribution. The model runs in Fig. 6 assume a uniform mass distributed across the entire residue while the modular approach in Fig. 17 accounts for the "coffee-ring" in a way that is also influenced by the size of the residue. That is, for smaller residue sizes the total area of the "coffee-ring" is smaller thus causing a higher mass density along the outer edge than for larger residues. Another influential factor is the particle stacking and conglomeration that is more prevalent on the hydrophilic resonator surface (Fig. 16b) which would lead to reduced effective masses and a ratio less than one.

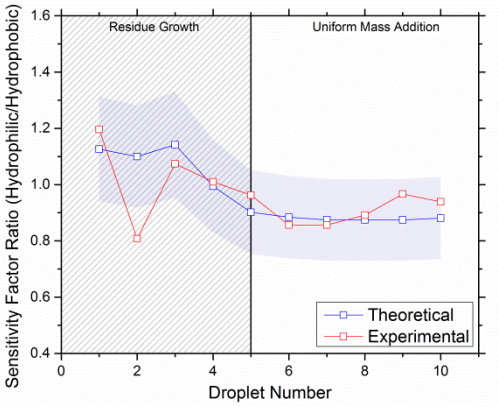

Fig. 17. Ratios of hydrophilic sensitivity to hydrophobic sensitivity on a per droplet basis for both theoretical and experimental results. After the initial residue growth stage, both theoretical and experimental results fluctuate around a ratio of 0.9. Filled area shows 95% confidence interval of theoretical model.

6. Conclusions

Bulk acoustic mode resonators show potential for high sensitivity mass sensing but consideration of their spatial sensitivity is necessary. Sensitivity to both mass and spatial distribution on the resonator was modelled and confirmed experimentally for the square extensional mode using piezoresistive sensing of electrostatically actuated MEMS resonators.

Three analytical sensitivity models were introduced with varying levels of complexity to investigate the implications of shape and area on sensitivity for a specific actuation mode. A modular approach was used to aptly compare the spatial sensitivity model to experimental results.

Three distinct stages of sensitivity were introduced covering initial residue growth, uniform mass addition, and particle stacking. The effects were observed regardless of surface treatment and based primarily on mass addition and distribution. The hydrophilic surface showed a larger degree of particle stacking and conglomeration when inspected with an SEM.

Potential improvements to the presented model focus around the assumptions made during the derivations. Incorporating non-homogeneous densities and non-uniform residue thicknesses would allow for a more accurate modelling potential for situations such as the “coffee-ring” effect (beyond the current approach). Furthermore, examining the particular case of a coupled resonator-particle system [28] for low particle attachment stiffness may explain the large fluctuations in resonant frequency during the particle stacking phase.

Experimentally, using a cleaner (*i.e.* fewer contaminants) particle source would provide more accurate comparisons and reproducible results since remaining the differences can be explained by a simple gain error.

Acknowledgements

The authors would like to thank A. Dickerson for assistance with the mechanical microbalance measurements. ATZ thanks the Natural Sciences and Engineering Research Council of Canada, the Sir Winston Churchill Society of Edmonton, and the Cambridge Trust for funding of the PhD degree.

References

[1] A.A. Seshia, M. Palaniapan, T.A. Roessig, R.T. Howe, R.W. Gooch, T.R. Schimert and S. Montague, "A vacuum packaged surface micromachined resonant accelerometer," *IEEE J. Microelectromech. S.*, vol. 11, no. 6, pp. 784-793, 2002.

[2] M. Koskenvuori, V. Kaajakari, T. Mattila and I. Tittonen, "Temperature measurement and compensation based on two vibrating modes of a bulk acoustic mode microresonator," in *IEEE 21st Int. Conf. Micro Electro Mechanical Systems*, Tucson, 2008.

[3] K.L. Ekinci and M.L. Roukes, "Nanoelectromechanical systems," *Rev. Sci. Instrum.*, vol. 76, no. 6, p. 061101, 2005.

[4] V.M. Mecea, "From quartz crystal microbalance to fundamental principles of mass measurements," *Anal. Lett.*, vol. 38, no. 5, pp. 753-767, 2005.

[5] IPCC, "Climate change 2013: the physical science basis. Contribution of working group I to the fifth assessment report of the intergovernmental panel on climate change," Cambridge University Press, Cambridge, 2013.

[6] D.W. Dockery, C A. Pope, X. Xu, J.D. Spengler, J.H. Ware, M.E. Fay, B.G. Ferris, Jr., and F.E. Speizer, "An association between air pollution and mortality in six U.S. cities," *N. Engl. J. Med.*, vol. 329, pp. 1753-1759, 1993.

[7] D.M. Holstius, A. Pillarisetti, K.R. Smith and E. Seto, "Field calibrations of a low-cost aerosol sensor at a regulatory monitoring site in California," *Atmos. Meas. Tech.*, vol. 7, pp. 1121-1131, 2014.

[8] J. Burkart, G. Steiner, G. Reischl, H. Moshammer, M. Neuberger and R. Hitzenberger, "Characterizing the performance of two optical particle counters (Grimm OPC1.108 and OPC1.109) under urban aerosol conditions," *J. Aerosol Sci.*, vol. 41, no. 10, pp. 953-962, 2010.

[9] C.A. Pope, III, and D.W. Dockery, "Health effects of fine particulate air pollution: lines that connect," *J. Air & Water Manage. Assoc.*, vol. 56, no. 6, pp. 709-742, 2006.

[10] G. Oberdörster, E. Oberdörster and J. Oberdörster, "Nanotoxicology: an emerging discipline evolving from studies of ultrafine particles," *Environ. Health Perspect.*, vol. 113, no. 7, pp. 823-839, 2005.

[11] R.L. Chuan, "Rapid measurement of particulate size distribution in the atmosphere," in *Fine Particles: Aerosol Generation, Measurement, Sampling, and Analysis*, B.Y.H. Liu, Ed. New York: Academic Press, Inc., 1976, pp. 763-766.

[12] J.P. Black, A. Elium, R.M. White, M.G. Apte, L.A. Gundel and R. Cambie, "MEMS-enabled miniaturized particulate matter monitor employing 1.6 GHz aluminum nitride thin-film bulk acoustic wave resonator (FBAR) and thermophoretic precipitator," in *Ultrasonics Symposium*, New York, 2007.

[13] I. Paprotny, F. Doering, P.A. Solomon, R.M. White and L.A. Gundel, "Microfabricated air-microfluidic sensor for personal monitoring of airborne particulate matter: design, fabrication, and experimental results," *Sens. Actuators A*, vol. 201, pp. 506-516, 2013.

[14] E. Mehdizadeh, J.C. Wilson, A. Hajjam, A. Rahafrooz and S. Pourkamali, "Aerosol impactor with embedded MEMS resonant mass balance for real-time particulate mass concentration monitoring," in *Int. Conf. Solid State Sensors, Actuators, and Microsystems*, Barcelona, 2013.

[15] A. Prasad, A.T. Zielinski, M. Kalberer, R.L. Jones and A.A. Seshia, "Studying particulate adsorption by drying droplets on a micromechanical elecro-acoustic resonator," in *28th European Frequency and Time Forum,* Neuchâtel, 2014.

[16] V. Kaajakari, T. Mattila, A. Oja, J. Kiihamäki and H. Seppä, "Square-extensional mode single-crystal silicon micromechanical resonator for low-phase-noise oscillator applications," *IEEE Electron Device Lett.*, vol. 25, no. 4, pp. 173-175, 2004.

[17] J.E-Y. Lee, Y. Zhu and A.A. Seshia, "A bulk acoustic mode single-crystal silicon microresonator with a high-quality factor," *J. Micromech. Microeng.*, vol. 18, no. 6, p. 064001, 2008.

[18] T. Mattila, J. Kiihamäki, T. Lamminmäki, O. Jaakkola, P. Rantakari, A. Oja, H. Seppä, H. Kattelus and I. Tittonen, "A 12 MHz micromechanical bulk acoustic mode oscillator," *Sens. Actuators A*, vol. 101, no. 1, pp. 1-9, 2002.

[19] J.E-Y. Lee, B. Bahreyni, Y. Zhu and A.A. Seshia, "Ultrasensitive mass balance based on a bulk acoustic mode single-crystal silicon resonator," *Appl. Phys. Lett.*, vol. 91, p. 234103, 2007.

[20] H. Campanella, E. Martincic, P. Nouet, A. Uranga and J. Esteve, "Analytical and finite-element modelling of localized-mass sensitivity of thin-film bulk acoustic-wave resonators (FBAR)," *IEEE Sens. J*, vol. 9, no. 8, pp. 892-901, 2009.

[21] A.T-H. Lin, J.E-Y. Lee, J. Yan and A.A. Seshia, "Methods for enhanced electrical transduction and characterisation of micromechanical resonators," *Sens. Actuators A*, vol. 158, no. 2, pp. 263-272, 2010.

[22] *SOIMUMPs Design Handbook*, 8th ed., MEMSCAP Inc., Durham, NC, 2011.

[23] P.J. Yunker, T. Still, M.A. Lohr and A.G. Yodh, "Suppression of the coffee-ring effect by shape-dependent capillary interactions," *Nature*, vol. 476, pp. 308-311, 2011.

[24] M.F. Guasti, "Analytic geometry of some rectilinear figures," *Int. J. Math. Educ. Sci. and Technol.*, vol. 23, no. 6, pp. 895-913, 1992.

[25] R. Maboudian, W.R. Ashurst and C. Carraro, "Self-asssembled monolayers as anti-stiction coatings for MEMS: characteristics and recent developments," *Sens. Actuators A*, vol. 82, no. 1, pp. 219-223, 2000.

[26] A.T-H. Lin, "Electrically addressed silicon microresonators for biochemical sensing," Ph.D. dissertation, Dept. Eng., Univ. Cambridge, Cambridge, UK, 2011.

[27] GIMP, *GIMP: GNU Image Manipulation Program*" [Online]. Available: www.gimp.org. [Accessed 2014].

[28] G.L. Dybwad, "A sensitive new method for the determination of adhesive bonding between a particle and a substrate," *J. Appl. Phys.*, vol. 58, no. 7, pp. 2789-2790, 1985.